

Article

The Eulerian–Lagrangian Approach for the Numerical Investigation of an Acoustic Field Generated by a High-Speed Gas-Droplet Flow

Valeriia G. Melnikova ^{1,2,*} , Andrey S. Epikhin ^{1,2} and Matvey V. Kraposhin ^{1,3} 

¹ Ivannikov Institute for System Programming of the Russian Academy of Sciences, 109004 Moscow, Russia; andreyepikhin@ispras.ru (A.S.E.); m.kraposhin@ispras.ru (M.V.K.)

² Special Machinery Department, Bauman Moscow State Technical University, 105005 Moscow, Russia

³ Keldysh Institute of Applied Mathematics of the Russian Academy of Sciences, 125047 Moscow, Russia

* Correspondence: vg-melnikova@yandex.ru

Abstract: This paper presents the Eulerian–Lagrangian approach for numerical modeling of high-speed gas-droplet flows and aeroacoustics. The proposed hybrid approach is implemented using the OpenFOAM library and two different methods. The first method is based on a hybrid convective terms approximation method employing a Kurganov–Tadmor and PIMPLE scheme. The second method employs the regularized or quasi-gas dynamic equations. The Lagrangian part of the flow description uses the OpenFOAM cloud model. Within this model, the injected droplets are simulated as packages (parcels) of particles with constant mass and diameter within each parcel. According to this model, parcels moving in the gas flow could undergo deceleration, heating, evaporation, and breakup due to hydrodynamic instabilities. The far-field acoustic noise is predicted using Ffowcs Williams and Hawking’s analogy. The Lagrangian model is verified using the cases with droplet evaporation and motion. Numerical investigation of water microjet injection into the hot ideally expanded jet allowed studying acoustic properties and flow structures, which emerged due to the interaction of gas and liquid. Simulation results showed that water injection with a mass flow rate equal to 13% of the gas jet mass flow rate reduced the noise by approximately 2 dB. This result was in good coincidence with the experimental observations, where maximum noise reduction was about 1.6 dB.

Keywords: Eulerian–Lagrangian approach; water droplets; particle; jet; quasi-gas dynamic equations; aeroacoustics; OpenFOAM



Citation: Melnikova, V.G.; Epikhin, A.S.; Kraposhin, M.V. The Eulerian–Lagrangian Approach for the Numerical Investigation of an Acoustic Field Generated by a High-Speed Gas-Droplet Flow. *Fluids* **2021**, *6*, 274. <https://doi.org/10.3390/fluids6080274>

Academic Editor: Mehrdad Massoudi

Received: 11 June 2021

Accepted: 30 July 2021

Published: 4 August 2021

Publisher’s Note: MDPI stays neutral with regard to jurisdictional claims in published maps and institutional affiliations.



Copyright: © 2021 by the authors. Licensee MDPI, Basel, Switzerland. This article is an open access article distributed under the terms and conditions of the Creative Commons Attribution (CC BY) license (<https://creativecommons.org/licenses/by/4.0/>).

1. Introduction

One of the most important problems in the aerospace field is the minimization of acoustic noise from jet engines [1]. The main source of noise from high-speed turbulent jets is hydrodynamic instabilities, which lead to the emergence of forces acting from the flow on the surrounding environment. In addition to large-scale turbulent structures, other noise sources can be mentioned, such as small-scale turbulence, Mach waves, and resonating elements of the flow [2–5]. Currently, various passive and active methods are used to reduce noise from jets. Essentially, these approaches dwindle the full energy of the jet and destruct coherent structures, emerging at the nozzle’s outflow of combustion products. Water injection into the hot gas jet zone is one of these methods. This approach was studied in papers [6–9]. Water droplets absorb kinetic energy from the gas flow due to resistance and thermal energy due to heat transfer and evaporation processes. The corresponding spatial changes in gas-dynamic fields lead to the destruction of flow structure. Usually, the practical application of these approaches involves detailed complex and expensive experimental studies of gas-dynamic and acoustic fields for small-scale models [8–11]. It is also worthwhile to mention studies that are devoted to hydrodynamic investigation

of liquid drops streamed from various micronozzles [12–14]. These investigations can be used as validation data for new mathematical models, as well as boundary conditions for droplet-flow models.

Recently, a fundamental understanding of the physical processes described above was supplemented with numerical simulation methods. Three methods of jet-noise prediction while accounting for water injection could be distinguished: semi-empirical models that combine a large amount of experimental data with the theory of similarity [15], methods of computational aero-gas-dynamics and acoustics using direct numerical simulation, and hybrid strategies. In hybrid strategies, the computational domain is divided into different subdomains.

Development and usage of numerical tools for adequate resolution and prediction of the aforementioned phenomena are complicated by the range of factors—local inhomogeneity of the Mach number, the difference in spatially temporal scales, presence of multiple phases, atomization of water jets, chemical reactions, interphase mass transfer, the reflection of shock waves, etc. The most commonly used methods in practical application are the finite volume method (FVM) and volume of fluid (VOF) [16,17]. However, such methods are very computationally expensive if applied to complex multiscale problems. The authors of [18] proposed a less computationally expensive Eulerian–Lagrangian approach with a point approximation of droplets. The entrainment effects in an evaporating turbulent jet atomizer were studied in the work. Sigma-Y models with transport equations for mass fraction and interphase surface-area concentration could replace the Lagrangian description of a droplet flow [19]. Reduced order models were used to reduce computational costs for computational aero-acoustic problems [20,21]. In these papers, coherent structures of jet flow were identified using the proper orthogonal decomposition method. Coupled simulation of gas-droplet jet flow and acoustics appears in a few studies. The authors in [22] used the two-fluid model (Euler approach) implemented in ANSYS software to simulate multiphase flow with water injection. However, droplet evaporation was not taken into account in that study. Far-field noise was predicted using the Ffowcs Williams—Hawkings analogy (FW-H). The papers [23,24] presented a study on jet-noise reduction by air injection using a single-phase approximation. In [25], the effect of water injection on noise reduction was carried out using an analytical investigation. In [26], the authors solved the problem using the Lattice Boltzmann method (LBM). It was noted that the undoubted advantage of LBM over traditional methods of computational fluid dynamics was the simplicity of solving problems with complex geometry.

Therefore, the existing approaches discussed above are convenient for modeling independent effects or phenomena. However, most of the mentioned approaches are not suitable for modeling multiscale structures due to the complexity of implementation and high computational costs. The numerical approach implemented in [22] partially allows us to solve these problems. However, the high demands for computational resources, the closed source code, and commercial licensing restrictions make the problem of developing an appropriate numerical simulation method and its open-source implementation certainly are relevant. The proposal in this work for solving the problem of determining acoustic noise from a supersonic jet, taking into account water injection, is based on the less resource-intensive Eulerian–Lagrangian approach. Gas-droplet flow is divided into two models: continuous (Eulerian phase) and discrete (Lagrangian phase). The Eulerian system describes the flow of a supersonic hot jet. The flow interacts with the environment and water droplets, which are described by Lagrangian particles and account for evaporation and atomization. The FW-H acoustic analogy is used for far-field noise prediction. The open-source OpenFOAM package is selected as the main platform for the model implementation.

2. Governing Equations

2.1. Gas Phase

The Eulerian part of the model describes the nonreacting chemical and thermodynamic equilibrium flow of the gas mixture. Individual transport of the mixture com-

ponents is accounted through the motion of mixture with the mass-averaged velocity and relative movement of components through the diffusion mechanism. The influence of the dispersed phase on the continuous phase is accounted via source terms in the balance equations of mass, energy, and momentum. With account to the stated assumptions, the mathematical model of a continuum compressible gaseous medium consists of three-dimensional equations for turbulent supersonic and subsonic flow: a mass-balance Equation (1), momentum-balance Equation (2), energy-balance Equation (3), mixture-component transport (Equations (4) and (5)), and perfect gas equation of state (EOS) for each component of the mixture (6).

The mass-balance equation is:

$$\frac{\partial \rho}{\partial t} + \nabla \cdot (\rho \vec{U}) = \dot{\rho}_v, \tag{1}$$

where ρ is flow density, t is time, and $\dot{\rho}_v$ is a source term describing the mass transfer between the gas and droplet phases.

The momentum-balance equation is:

$$\frac{\partial (\rho \vec{U})}{\partial t} + \nabla \cdot (\vec{U} \rho \vec{U}) + \sum_i \rho_i^0 \vec{W}_i \vec{W}_i = \dot{\rho}_v \vec{U}_v + \nabla \cdot \hat{\sigma} - \nabla p + \rho \vec{g}, \tag{2}$$

where p is the mixture pressure, equal to the sum of components partial pressure; ρ_i^0 is flow density of the i th component; $\dot{\rho}_v \vec{U}_v$ is a source term that describes momentum exchange between gas and droplets phases; and \vec{g} is the gravity.

The energy-conservation equation is:

$$\frac{\partial (\rho e)}{\partial t} + \nabla \cdot (\rho e \vec{U}) + \sum_i \nabla \cdot \vec{W}_i \rho_i^0 e_i + \nabla \cdot (p \vec{U}) = -\nabla \cdot (\hat{\sigma} \cdot \vec{U}) - \nabla \cdot \vec{q} + \dot{\rho}_v e_v, \tag{3}$$

where e is the total energy, $\dot{\rho}_v e_v$ is a source term that describes the energy exchange between gas and droplets, $\hat{\sigma} = \mu (\nabla \vec{U} + (\nabla \vec{U})^T) - \frac{2}{3} \mu I \nabla \cdot \vec{U}$ is the stress tensor, μ is dynamic viscosity, and I is unit tensor.

The heat-flux vector is calculated in accordance with Fourier's law: $\vec{q} = -\lambda \nabla T$, where T is the gas mixture temperature, and λ is mixture thermal conductivity coefficient:

$$\lambda = \frac{\mu C_p}{Pr} + \frac{\mu_{SGS} C_p}{Pr_{SGS}}, C_p = \left(\frac{\partial h}{\partial T} \right)_p, \nabla T = \frac{\nabla h}{C_p},$$

where Pr is the Prandtl number; Pr_{SGS} is subgrid Prandtl number; $\mu_{sgs} = (C_s \Delta)^2 |S|$ is the subgrid viscosity, where Δ is filter size; C_s is an empirical constant (Smagorinsky constant): $|S| = (2S_{ij}S_{ij})^{1/2}$, $S_{ij} = \frac{1}{2} \left(\frac{\partial U_j}{\partial x_i} + \frac{\partial U_i}{\partial x_j} \right)$. Mixture-specific enthalpy h is the weighted sum of specific enthalpies of its components:

$$h = \sum_i Y_i h_i,$$

where $Y_i = \frac{\rho_i^0}{\rho}$ is mass fraction of the i th component. Transport of the mixture components is governed by:

$$\frac{\partial \rho Y_i}{\partial t} + \nabla \cdot (\rho Y_i \vec{U}) + \rho_i^0 \nabla \cdot \vec{W}_i = \dot{\rho}_i, \tag{4}$$

where $\dot{\rho}_i$ is a source term that describes generation or destruction of a species; namely, generation of water vapor due to evaporation of droplets.

The mass fractions of mixture components follow next algebraic rule:

$$\sum_i Y_i = 1. \tag{5}$$

The mass-average mixture velocity $\vec{U} = \frac{\sum_i \rho_i^0 \vec{U}_i}{\rho}$ and relative velocity of *i*th component $\vec{W}_i = \vec{U} - \vec{U}_i$ are defined as:

$$\sum_i Y_i \vec{W}_i = 0.$$

Diffusion approximation is used to calculate mixture components relative velocities:

$$\rho_i^0 \vec{W}_i = -D_i \nabla \rho_i^0,$$

where $D_i = \frac{\nu_i}{Sc}$ is the diffusion coefficient of the *i*th component.

Each component of the gaseous mixture is an ideal gas with a constant molar mass:

$$p_i = \rho_i R_i T, \tag{6}$$

where p_i is the *i*th component pressure, ρ_i is thermodynamic density of the *i*th component, and R_i is ideal gas constant.

The model is implemented as two OpenFOAM applications based on classical and quasi-gas dynamic (QGD) systems of equations. The first solver, named reacting LagrangianPimpleCentralFoam (RLPCF), uses the hybrid Kurganov–Tadmor technique based on the flow model for an arbitrary EOS [27]. The second numerical algorithm is implemented as reactingLagrangianQGDfoam (RLQGD) solver, and is based on regularized or quasi-gas dynamic equations [28]. As an extension of the classical system of Navier–Stokes equations, the QGD system contains regularizing terms that are proportional to a coefficient with dimension of time. When this coefficient tends to zero, the QGD system of equations reduces to the conventional system for perfect gas mixture motion based on Navier–Stokes equations; e.g., (1)–(6). Detailed information about the regularized equations employed in this study can be found in the papers [29–31].

2.2. Liquid Phase

The model of the liquid-droplet system is based on the OpenFOAM cloud model formulated using the Lagrangian approach. Within this model, a system of liquid droplets is represented as a cloud of so-called parcels or bundles of droplets with similar mass. Such representation allows us to save computational resources for real applications in which the resolution of each droplet is not feasible (the total number of particles is larger than 10^7).

Each parcel is characterized by the geometric center of masses x_p of spherical particles with diameter D_p , density ρ_p , mass $m_p = \frac{1}{6} \rho_p \pi D_p^3$, temperature T_p , and velocity \vec{U}_p . The evolution of each particle is governed by kinematic Equation (7), momentum-balance Equation (8), mass-balance Equation (12), and energy-balance Equation (13). The resultant force acting on a particle is the sum of the drag force from the fluid phase (\vec{F}_D) and gravity force (\vec{F}_G).

$$\frac{d\vec{x}_p}{dt} = \vec{U}_p, \tag{7}$$

$$m_p \frac{d\vec{U}_p}{dt} = \sum \vec{F}_i = \vec{F}_D + \vec{F}_G = m_p \frac{\vec{U} - \vec{U}_p}{\tau_p} + m_p \vec{g} \left(1 - \frac{\rho}{\rho_p} \right). \tag{8}$$

The drag force is formulated through the relaxation time of a particle—the time it takes for a particle to respond to changes in the local flow velocity:

$$\tau_p = \frac{4}{3} \frac{\rho_p D_p}{\rho \cdot C_D \cdot \left| \vec{U} - \vec{U}_p \right|}. \tag{9}$$

The drag coefficient module $C_D Re_p$ is calculated via empirical Putnam dependency [32]:

$$C_D Re_p = \begin{cases} 0.424 \cdot Re_p, & Re_p > 1000 \\ 24 \cdot \left(1 + \frac{1}{6} Re_p^{2/3} \right), & Re_p \leq 1000 \end{cases} \tag{10}$$

The particle Reynolds number is defined as:

$$Re_p = \frac{\rho \left| \vec{U} - \vec{U}_p \right| D_p}{\mu}. \tag{11}$$

The model also includes a drop mass-balance equation:

$$\frac{dm_p}{dt} = \dot{m}_p = \frac{m_p}{\tau_e}, \tag{12}$$

where τ_e is evaporation relaxation time.

The drop energy-balance equation is:

$$m_p C_{pp} \frac{dT_p}{dt} = q_T - \dot{m}_p L, \tag{13}$$

where C_{pp} is the particle-specific heat capacity at constant pressure, T_p is the particle temperature, q_T is total heat flux through the particle outer surface, and L is the latent heat of vaporization.

It is assumed that injected water is already divided into separate droplets at the point of injection; i.e., the cloud of droplets with a predefined diameter density function is already formed. The droplet size distribution for mean droplet diameter d_{mean} was set according to the generalized normal distribution (Figure 1) [12,13]. The normal rebound model (elasticity coefficient is equal to one) is used as a model of particle interaction with the impermeable walls of a computational domain. If particles reach the inlet or outlet boundaries of a computational domain, then they are removed from computations.

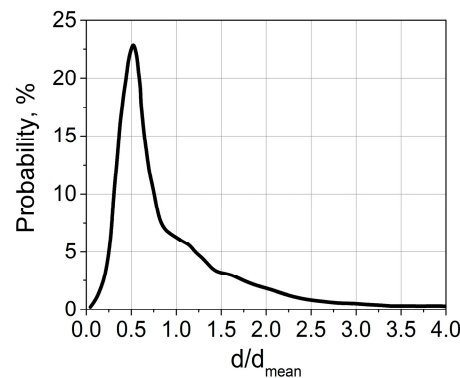


Figure 1. Rescaled droplet size distribution in a parcel.

The droplet-breakup mechanism due to hydrodynamic instabilities is accounted for using the Taylor analogy breakup (TAB) model [33], which is based on Taylor’s analogy between an oscillating distorting droplet and a spring-mass system. When the speed of

a parcel increases, the number of droplets grows. On the other hand, drops with smaller diameter evaporate faster. The final number of fragments after a drop breakup depends on the critical Weber number, which equal to six in this model. The increase of the critical Weber number leads to a reduction of the evaporation rate since droplets break slower, and hence have a larger diameter.

2.3. Gas and Liquid Phase Coupling

During the motion, particles interact with the gas flow and exchange mass, momentum, and energy via processes of viscous drag, heating, and evaporation. The energy transfer rate between models is estimated using semiempirical closure relations between surface heat flux and near-droplet temperature difference:

$$q_T = htc \cdot S_p \cdot (T_{sp} - T),$$

where $S_p = \pi D_p^2$ is the drop surface area, $htc = \frac{Nu \cdot \lambda}{D_p}$ is the heat-transfer coefficient, λ is the thermal conductivity of the flow, and $T_{sp} = \frac{2}{3}T_p + \frac{1}{3}T$ is the drop surface temperature.

The heat-transfer coefficient for a sphere in a flow of viscous gas is calculated using the Ranz–Marshall correlation [34]:

$$Nu = 2 + 0.6 \cdot \sqrt{Re} \cdot \sqrt[3]{Pr},$$

where $Pr = \frac{c_p \cdot \mu}{\lambda}$ is the Prandtl number, and C_p is the flow-specific heat capacity at constant pressure.

The evaporation of droplets is accounted via the Spaulding phase-change model [18], which considers diffusive mass flux of liquid molecules from the surface of the spherical droplet due to the saturated vapour concentration gradient.

2.4. Acoustic Prediction

The far-field acoustic pressure is predicted using the Farassat 1A formulation [35,36] of the Ffowcs Williams—Hawking analogy implemented in the libAcoustics library [37,38].

The sound pressure level (SPL) is calculated as:

$$SPL(\text{dB}) = 20 \log_{10} \left(p_{rms} / p_{ref} \right),$$

where p_{rms} is the root mean square of sound pressure; and p_{ref} is the reference sound pressure, which is equal to $2 \cdot 10^{-5}$ Pa.

3. Verification and Validation

The Eulerian part of the model for both of the system equations was verified by solving the various problems such as: (a) shock tube and other discontinuity evolution problems [27,28], (b) the flow around the forward and backward step with super- and subsonic velocities [28,39], (c) flow around blunt bodies at trans- and supersonic velocities [27,28,39], and d) hydrodynamic instabilities development and acoustic noise generation by a transonic jet [40,41]. The libAcoustics library of far-field noise analysis was successfully tested for a number of models (monopole, dipole) and experimental problems [37,40,41]. The verification of the droplet-dynamics model is presented in the next two sections.

3.1. Droplet Evaporation

The default OpenFOAM liquid evaporation model and Spalding model [18] have been verified. According to the analytical solution, the time the droplet needs to vaporize completely is proportional to the square of the droplet radius (r^2 -law). The case was considered to have verified the r^2 -law when the stationary water droplet (diameter of 0.0017 m, mass of $2571 \cdot 10^{-9}$ kg) evaporated in a very large volume without the influence

of external forces and heat exchange. The environmental temperature (293 K) and pressure (101,300 Pa) were constant. The numerical simulation results are presented in Figure 2a.

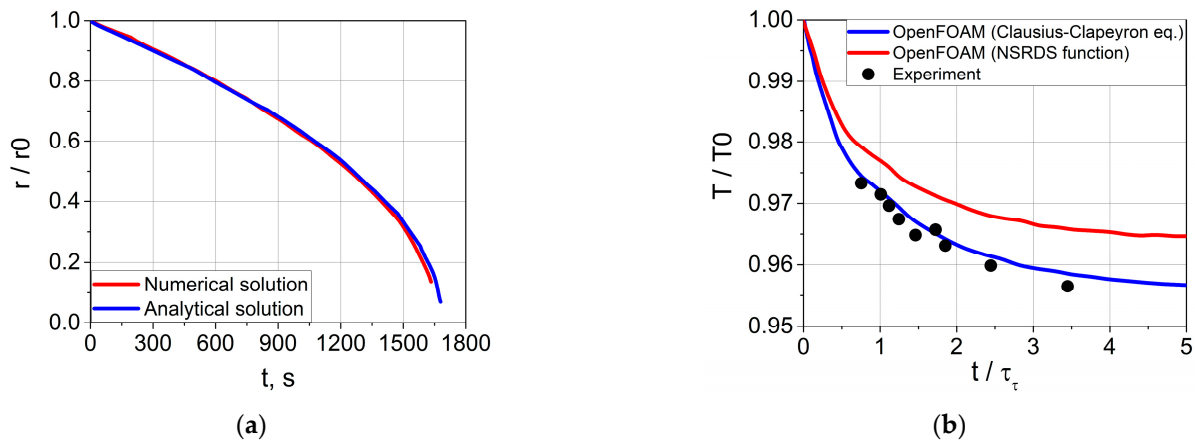


Figure 2. Drop evaporation tests: (a) particle size dependence over time; (b) temperature dependence over time.

In another test case, the water droplet evaporation was accompanied by the decline of thermal energy (temperature). The water droplet with a temperature of 301.45 K fell freely. External temperature was equal to 301.45 K and pressure was 101,300 Pa, and the air relative humidity was set to 0.22. Two variants of expression for saturated pressure calculations were used: the NSRDS function and the Clausius–Clapeyron equation. Results of the current simulation were compared with a reference simulation and with the experimental results in [18] (see Figure 2b).

Calculation of the isothermal droplet evaporation process using the implemented model showed that the droplet radius evolution curve differed from r^2 law by less than 10% (see Figure 2a) in the time interval of 0–1000 s. For the second case, the temperature time dependence of the falling droplet was calculated and compared with experimental measurements. The results of the calculations differed from the experiment by less than 5% (Figure 2b).

3.2. Droplet Movement

The problem of droplet motion in gas is considered to validate the momentum model (Figure 3). During the motion, a droplet exchanges momentum with the surrounding gas, and as a result, it changes its shape, and can break into several smaller droplets. In turn, this mechanism affects the processes of mass and heat exchange and ultimately influences the acoustic noise level.

The droplet motion was considered with initial velocity U_d equal to 16 m/s in a gas flow with uniform velocity field $U_g = 59$ m/s, temperature of 300 K, and a pressure of 0.5 GPa. The drop diameter was $d = 170 \cdot 10^{-6}$ m, the mass was $m_d = 2571 \cdot 10^{-9}$ kg, and the temperature was $T_d = 300$ K. The simulation area dimensions were $0.028 \times 0.02 \times 0.001$ m,

the Reynolds Number was $Re = 669$, the Weber number was $We = \frac{\rho \cdot |\vec{U}_g - \vec{U}_p|^2 \cdot d}{\sigma} = 36$, and the surface tension σ was equal to 0.02 kg/s².

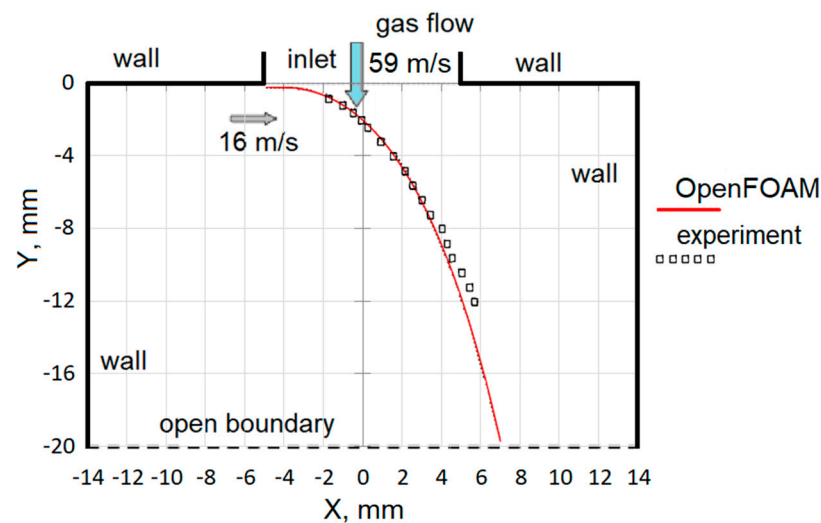


Figure 3. Problem statement: droplet trajectory in the flow.

The results showed satisfactory coincidence between the simulation and the experimental data [42]. It should be noted that mentioned differences between the reference and computed values could be further diminished by adjusting model coefficients. However, it did not seem necessary here because the typical practical problem statement includes many other uncertainties, which can impact the result of far-field noise prediction. The considered verification cases demonstrated overall correspondence of the model to basic physical mechanisms.

4. Jet-Noise Prediction with Water Microjet Injection

The far-field noise prediction of a high-speed jet with and without water microjet injection was considered as the validation case. Flow geometry and parameters matched the experimental study conducted by Greska [43]. Six micronozzles, each forming a water microjet supply, were evenly spaced around the gas nozzle exit. The acoustic pressure was measured with and without the presence of a water supply at a distance from the nozzle exit of about 30 diameters at different angles to the jet axis.

4.1. Computational Setup

When the exit diameter of the nozzle was $D = 0.04$ m, the jet of nonreacting gas with $\gamma = 1.338$ was ideally expanded. The following parameters of the jet flow were used: $U_j = 880$ m/s, $T_j = 624$ K, $M_j = 1.8$, $Re_D = 640,000$. The nozzle pressure ratio (NPR) operating pressure was equal to 5.6. The diameter of the water injection micronozzle was 800 μm . Micronozzles were installed at an angle of 60° upstream of the gas jet. The mass flux of the microjets' water supply was 13% of the gas jet. The water injection was modelled from conical micronozzles at an angle of 20° . The flow of liquid droplets was resolved with a Lagrangian model density of 10^6 parcels per second. The models based on the Eulerian–Lagrangian approach required an initial distribution of size of droplets, but previous experimental study [43] did not provide such information. The common way to define initial sizes of droplets is to use Rosin–Rammler distribution with the volume median droplet diameter (D_{50}) as a parameter. It was established in a previous investigation [13] that droplet size was insensitive to liquid viscosity. The volume median diameter can be estimated as $D_{50}/b \sim We^{-1/3}$, where b is the characteristic length, $We = \rho_{liq} U_{liq}^2 b / \sigma$. The plot of the used droplet size distribution is presented in Figure 1.

The computational domain (Figure 4) was a rectangular parallelepiped in which the outlet boundary was placed at the distance $80D$ between opposite sides in the jet axis direction, and at a distance of $20D$ in other directions. The inlet boundary corresponded to the gas nozzle exit of circular shape, with the center located in the origin of the coordinates (Figure 4).

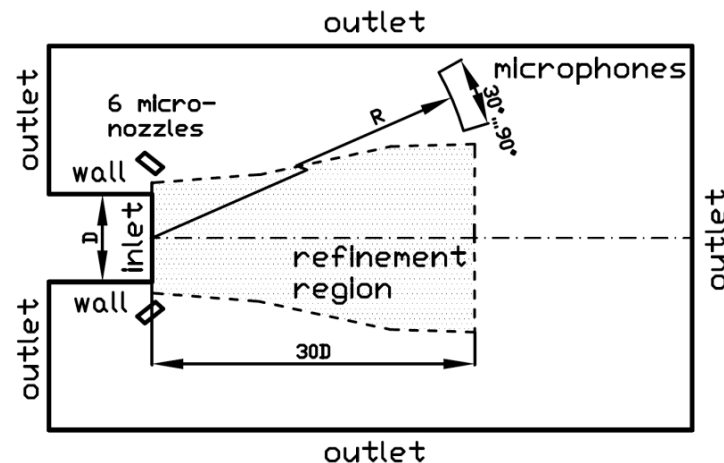


Figure 4. Computational domain and boundary conditions.

The computational mesh was refined in the region from the gas nozzle exit $30D$ downstream. According to the recommendations presented in [40,41], two meshes for each solver were constructed. It was shown in previous studies that two numerical algorithms required different mesh resolutions to simulate the instabilities arising from the mixing layer of a high-speed jet. The first mesh, with uniform refinement of 40 cells per diameter (CPD) in the region surrounding $30D$ of the jet and a total number of cells equal to 33.5 million was used for the QGD algorithm. Spatial resolution of 60 CPD in the jet core and 30 CPD in the remaining part of the refinement region was used for the second mesh. This mesh was used with the RLPCF solver. Both grids were uniform in the area of interaction between the hot jet and water droplets. The uniform grid remedied numerical problems arising in water–gas interaction region described in the paper [44].

The mass fraction of the air component equalled 1 in the internal field at the initial time. Gas with the conditions prescribed above was set on the inflow boundary. A turbulent pulsation of the velocity field equal to 2% was imposed on the inlet boundary. The Smagorinsky subgrid scale model with constant $C_s = 0.05$ and the Adams–Bashforth scheme for time discretization were used. The numerical schemes and regularized parameters for both RLPCF and RLQGD solvers are presented in detail in the papers [40,41].

Virtual microphones were placed at a distance of $R = 3.048$ m. The angle of microphone position θ varied from 30 to 90° to the jet axis and was measured from the downstream jet axis.

4.2. Near-Field Results

The near-field results were similar for both solvers. The axial distributions of the velocity field with and without water injection are presented in Figure 5. The paper [43] does not contain information about the jet centerline parameter distribution to validate numerical methods. Therefore, to check our numerical models, we used experimental data from the investigation conducted by Baars and Tinney [45], in which parameters at the nozzle exit section were similar to those specified in [43]: $M_j = 1.55$, $Re_D = 596,000$, $T_j = 735$ K. As can be seen from Figure 5, the computed values from the model setup [43] were in good qualitative agreement with experimental data [45].

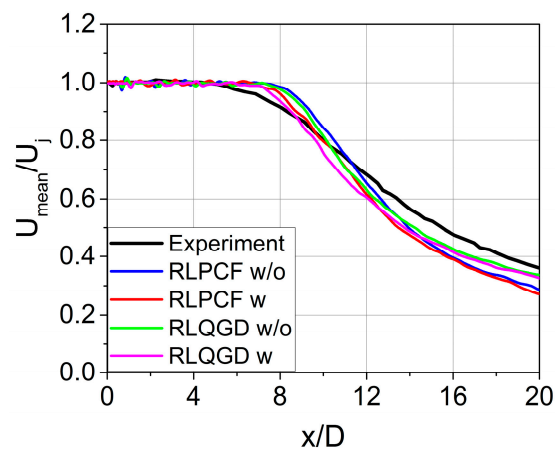


Figure 5. Axial distribution of the mean velocity field.

Typical flow structures for the RLPCF solver are presented in Figures 6–8. The mean streamwise velocity fields and the spatial distribution of the injected parcels are shown in Figures 6 and 7, respectively. The mass fraction of water is depicted in Figure 8. The initial and the final (end of simulation) droplet size distributions are presented in Figure 9a, and droplet diameter versus jet axis coordinate is plotted in Figure 9b.

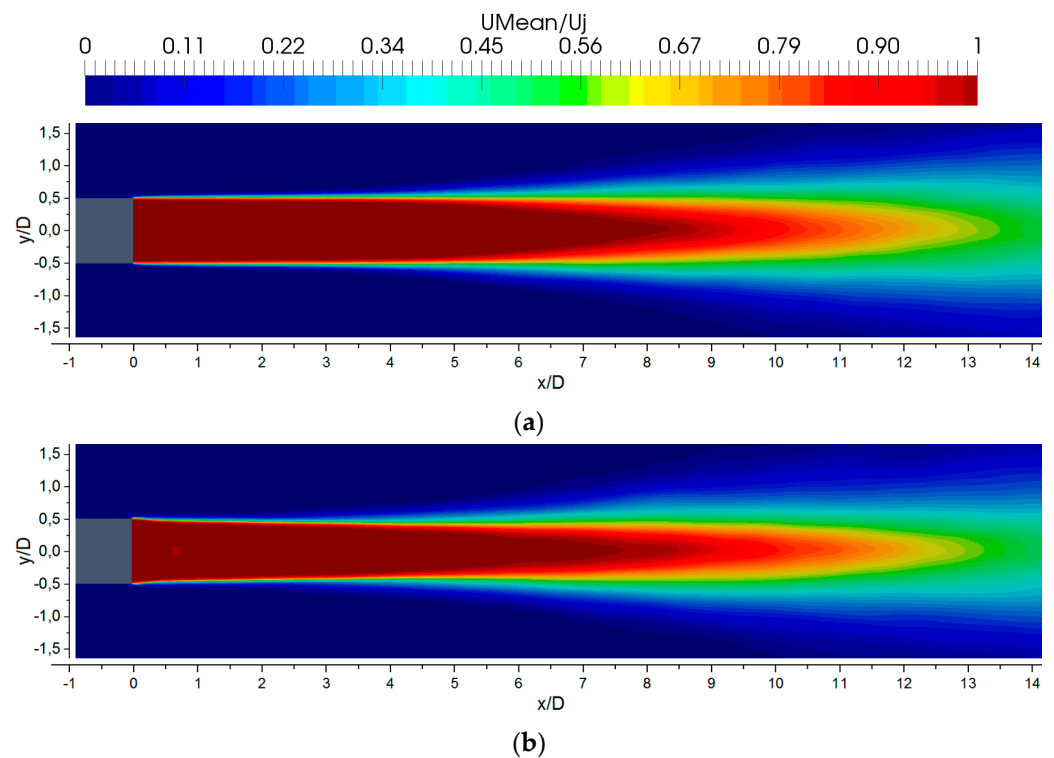


Figure 6. Mean velocity field: (a) normal jet; (b) with water injections.

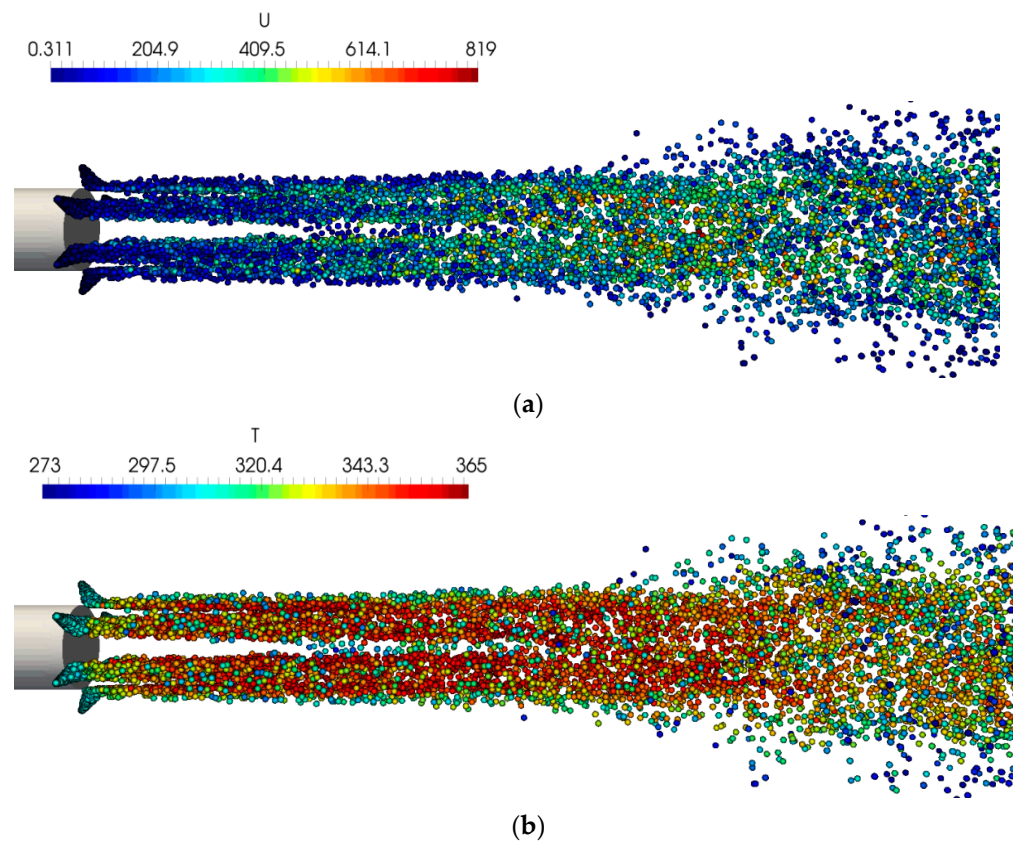


Figure 7. Injected parcels of water: (a) velocity; (b) temperature.

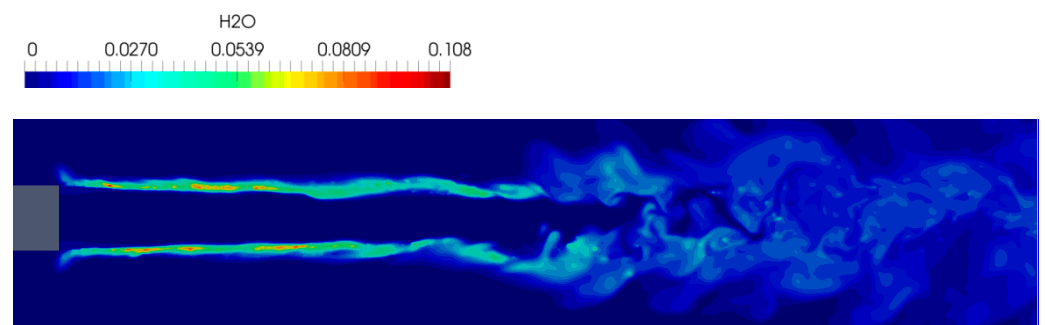


Figure 8. Instantaneous mass fraction of water (as mentioned in Equation (4)).

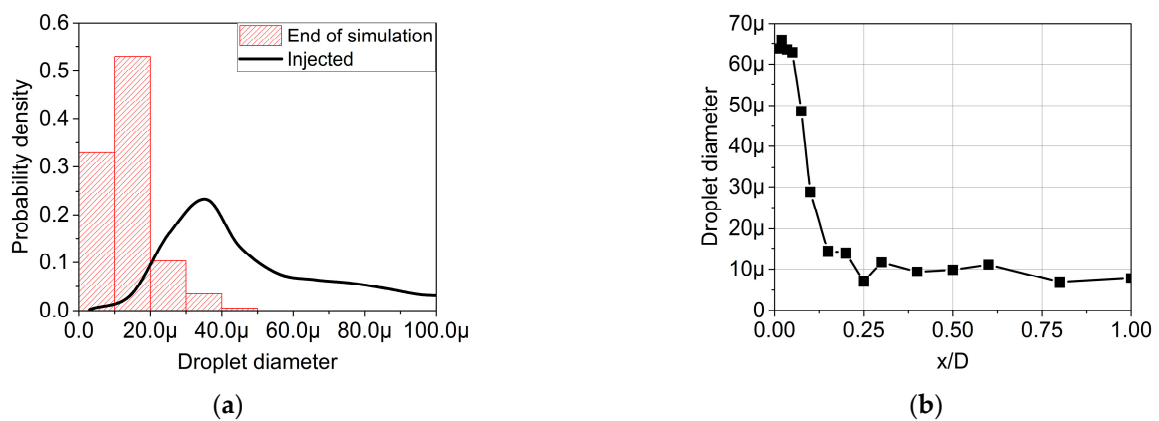


Figure 9. (a) Droplet size distribution at the injection and for the end of simulation; (b) droplet size along the x-direction.

The interaction of water microjets occurs in the shear layer of the gas jet. Droplets are rapidly breakup to a size of about 10 μm during the distance equal to one jet nozzle diameter in the axial direction. The further propagation of water parcels in the shear layer occurs their partial evaporation. It is found that about 20% of the mass fraction of water evaporated, while the size of the droplets significantly decreased compared to their initial sizes.

4.3. Acoustic Far-Field

Two open surfaces were constructed (they are schematically depicted in Figure 10) using recommendations for FW-H generations from [46,47] for jet-flow acoustic-pressure predictions. Control surfaces began 0.1D downstream of the inflow boundary and extended to 35D along the streamwise direction.

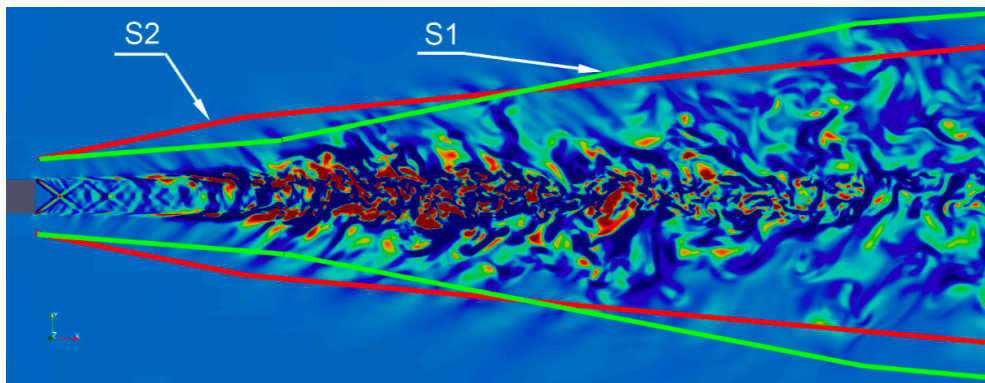


Figure 10. A scheme showing the two open control surfaces surrounding the jet (divergence of velocity contours are shown).

Simulation results of the overall sound-pressure level (OASPL) for the jet without water injection are presented in Figure 11a. Figure 11b illustrates the effect of the microjets influence on the OASPL of the ideally expanded jet in comparison with the experimental data. Figure 12 shows the far-field narrowband frequency noise spectra and a comparison with experiment data at $\theta = 90^\circ$ [43].

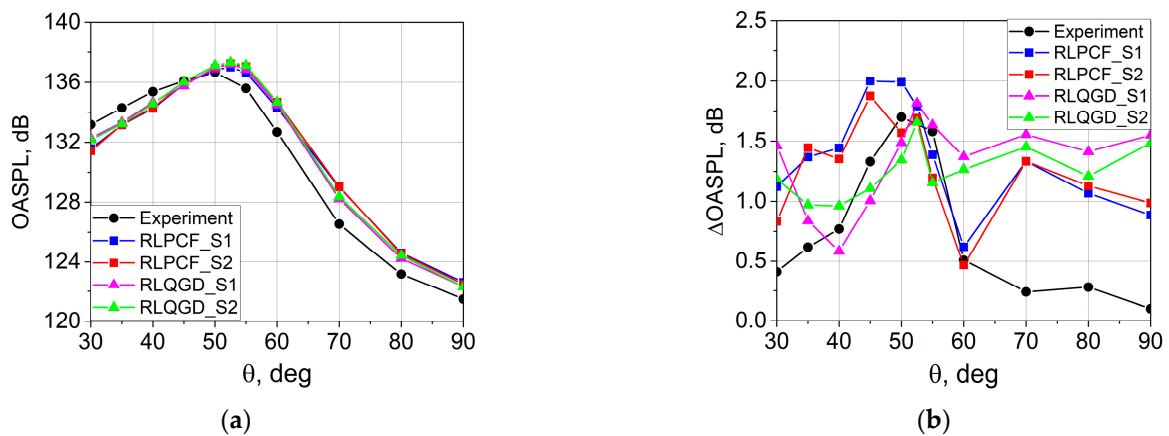


Figure 11. Directivity plot comparing noise fields of the ideally expanded jet: (a) OASPL in dB; (b) reduction of the OASPL at each angle.

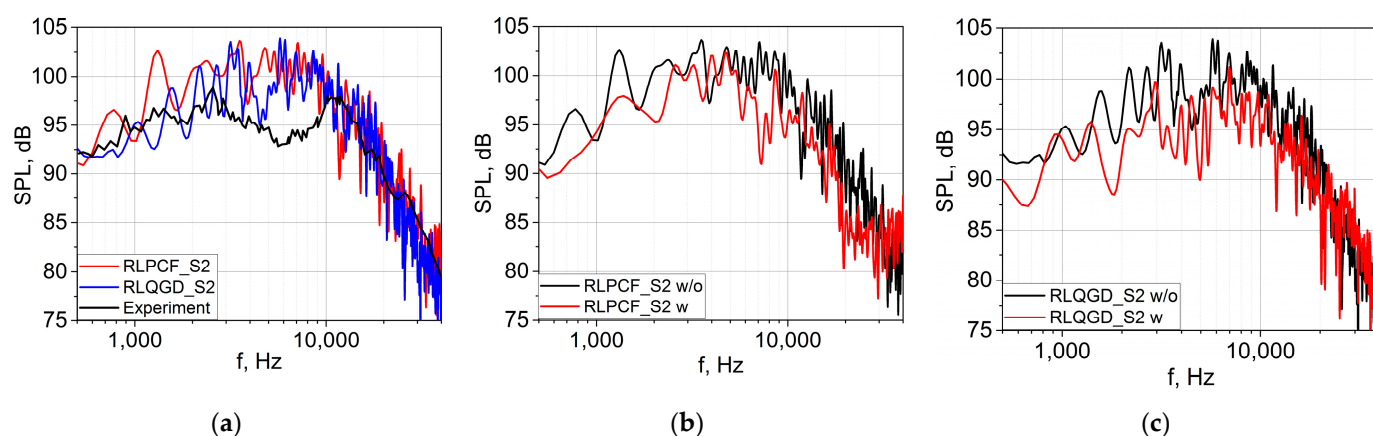


Figure 12. Narrowband frequency spectra at $\theta = 90^\circ$: (a) without water injection; (b) with the effect of water microjet injection calculated with the RLPCF solver; (c) with the effect of water microjet injection calculated with the RLQGD solver.

The results showed good quantitative agreement of the OASPL distribution and relatively satisfactory qualitative agreement of the OASPL difference in circumferential direction. The direction of maximum radiation magnitude was shifted by $2\text{--}3^\circ$ and was near 52.5° . The largest difference was about 2.5 dB at an angle of 70° . The comparison of narrowband spectra showed some overestimation of the calculated SPL, with experimental values near 6 kHz frequencies. According to the qualitative comparison, the QGD algorithm reproduced the spectrum better than the hybrid approach (RLPCF). Water microjet injection with a mass-flux ratio of 13% led to a small transformation of the structure and to the appearance of a weak shock-cell structure. Such changes caused redistribution in the intensity and direction of the pressure waves generated by the jet. In these conditions, water injection reduced the overall sound pressure level for an ideally expanded jet over an entire range of studied angles (Figure 11b). The injection of water microjets at $\theta = 90^\circ$ affected low frequencies mainly in this setup. Maximum noise reduction was observed in the range of $45\text{--}55^\circ$, and was equal to 1.75–2 dB. The discrepancy of ΔOASPL (the difference between OASPL w/o and w/water injection) for the calculated and experimental values was about 0.5–1.25 dB. A maximum discrepancy also was observed at an angle of 70° . These differences can be explained by uncertainty in the profile of the velocity field at the inflow boundary in the experiment. The insufficient grid resolution in the area of propagation of perturbations from the jet and the shape of the FW-H surfaces also could be the source of acoustics far-field prediction error. Thus, the numerical simulation results showed a satisfactory agreement with the results of the experiment conducted by Greshka [43].

5. Conclusions

In this study, a flow model encompassing a description of a multicomponent gas mixture, droplet cloud motion, evaporation, and interaction with the acoustic analogy was developed. The proposed mathematical model was implemented using the Eulerian–Lagrangian approach in OpenFOAM open-source package using two numerical approaches: (a) hybrid Kurganov–Tadmor and a PIMPLE algorithm; and (b) a QGD algorithm. Separate parts of the model were verified using problems with a known solution for water-droplet dynamics, gas dynamics, and acoustic-perturbation propagation. The whole model was validated with a case combining all three phenomena. In this case, the jet-noise reduction by water microjet injection was considered. The results obtained from the numerical simulations of far-field noise showed a satisfactory agreement with the experimental data. The calculated maximum noise reduction by water injection was 2 dB, while the experimental reduction was about 1.6 dB. The spatial direction in which the maximum reduction was observed also coincided with the experiment. This direction corresponded to the direction of maximum sound radiation. Simulation showed that the injected droplets' size changes at axial distances up to one nozzle diameter from the inlet plane downwind. Droplets'

velocity rapidly increases with the developing gas flow, leading to their breakup after injection. The final size of the droplets depends primarily on the gas flow velocity; i.e., among two factors (the breakup and evaporation), the first one plays the major role.

The calculations showed the importance of CFD tool application in numerical far-field acoustic noise numerical prediction in the presence of interaction between gas and liquid flows. According to the common notion regarding the general influence of cold droplets on the sound generated by hot jets, the mean energy of the gas flow is absorbed, and therefore, the OASPL reduces. However, it is worth noting that in some circumstances, the spatial interaction between two phases could lead to a redistribution of flow structure, yielding sustainable or even growing acoustic noise due to the emergence of sources of another type.

Similar problems, such as fuel injection in automobile engines, injector operation in steam boilers, or gas atomization of metal to produce powder for 3D printing, can be also solved using the proposed approach.

Author Contributions: Conceptualization, A.S.E. and M.V.K.; Software, V.G.M. and A.S.E.; Investigation, A.S.E. and V.G.M.; Visualization, A.S.E.; Writing—original draft, V.G.M. and A.S.E.; Writing—review & editing, M.V.K. All authors have read and agreed to the published version of the manuscript.

Funding: This research was supported by the Russian Science Foundation (project no. 19-11-00169).

Data Availability Statement: The hybrid solvers are available at GitHub <https://github.com/unicfdlab/hybridCentralSolvers.git> (accessed on 10 June 2021). Quasi-gas dynamic solvers: <https://github.com/unicfdlab/QGDsolver.git> (accessed on 10 June 2021). LibAcoustics library: <https://github.com/unicfdlab/libAcoustics.git> (accessed on 10 June 2021).

Acknowledgments: This work was carried out using computing resources of the federal collective usage center at the Complex for Simulation and Data Processing for Mega-Science Facilities at NRC “Kurchatov Institute”, <http://ckp.nrcki.ru/>.

Conflicts of Interest: The authors declare no conflict of interest. The funders had no role in the design of the study; in the collection, analyses, or interpretation of data; in the writing of the manuscript; or in the decision to publish the results.

References

1. Casalino, D.; Diozzi, F.; Sannino, R.; Paonessa, A. Aircraft noise reduction technologies: A bibliographic review. *Aerosp. Sci. Technol.* **2008**, *12*, 1–17. [\[CrossRef\]](#)
2. Crighton, D.G. Basic principles of aerodynamic noise generation. *Prog. Aerosp. Sci.* **1975**, *16*, 31–96. [\[CrossRef\]](#)
3. Tam, C.K.W.; Viswanathan, K.; Ahuja, K.K.; Panda, J. The sources of jet noise: Experimental evidence. *J. Fluid Mech.* **2008**, *615*, 253–292. [\[CrossRef\]](#)
4. Tam, C.K.W.; Shen, H.; Raman, G. Screech tones of supersonic jets from bevelled rectangular nozzles. *AIAA J.* **1997**, *35*, 1119–1125. [\[CrossRef\]](#)
5. Tam, C.K.W. Mach wave radiation from high-speed jets. *AIAA J.* **1984**, *47*, 2440–2448. [\[CrossRef\]](#)
6. Ignatius, J.; Sankaran, S.; Kumar, R.; Satyanarayana, T.; Chakravarthy, S. Suppression of jet noise during launch vehicle lift-off by water injection. *Int. J. Aeroacoustics* **2008**, *7*, 223–241. [\[CrossRef\]](#)
7. Washington, D.; Krothapalli, A. The role of water injection on the mixing noise supersonic jet. In Proceedings of the 4th AIAA/CEAS Aeroacoustics Conference, Toulouse, France, 2–4 June 1998; p. 2205.
8. Zoppellari, E.; Juvé, D. Reduction of supersonic jet noise by water injection. In Proceedings of the 4th AIAA/CEAS Aeroacoustics Conference, Toulouse, France, 2–4 June 1998; p. 2204.
9. Marchesse, Y.; Gervais, Y.; Foulon, H. Water injection effect on hot supersonic jet noise. *Comptes Rendus Mécanique* **2002**, *330*, 1–8. [\[CrossRef\]](#)
10. Krothapalli, A.; Venkatakrishnan, L.; Lourenco, L.; Greska, B.; Elavarasan, R. Turbulence and noise suppression of a high-speed jet by water injection. *J. Fluid Mech.* **2003**, *491*, 131–159. [\[CrossRef\]](#)
11. Norum, T.D. Reduction in multi component jet noise by water injection. In Proceedings of the 10th AIAA/CEAS Aeroacoustics Conference, Manchester, UK, 10–12 May 2004; p. 2976.
12. Labergue, A.; Gradeck, M.; Lemoine, F. Comparative study of the cooling of a hot temperature surface using sprays and liquid jets. *Int. J. Heat Mass Transf.* **2015**, *81*, 889–900. [\[CrossRef\]](#)
13. Kooij, S.; Sijts, R.; Denn, M.M.; Villermaux, E.; Bonn, D. What determines the drop size in sprays? *Phys. Rev. X* **2018**, *8*, 031019. [\[CrossRef\]](#)

14. Trang, C.; Ahmed, R.; Kaosar, M.G. Effect of density ratio on the dispersion of particles in a submerged liquid jet. *Comput. Part. Mech.* **2019**, *6*, 581–589. [[CrossRef](#)]
15. Kandula, M. Prediction of turbulent jet mixing noise reduction by water injection. *AIAA J.* **2008**, *46*, 2714–2722. [[CrossRef](#)]
16. Yin, C. Transient heating and evaporation of moving fuel droplets. *Energy Procedia* **2014**, *61*, 37–40. [[CrossRef](#)]
17. Zahoor, R.; Regvar, R.; Bajt, S.; Šarler, B. A numerical study on the influence of liquid properties on gas-focused micro-jets. *Prog. Comput. Fluid Dyn.* **2020**, *20*, 71–83. [[CrossRef](#)]
18. Barba, F.D.; Picano, F. Evaporation of dilute droplets in a turbulent jet: Clustering and entrainment effects. *arXiv* **2017**, arXiv:1703.05927v1.
19. Garcia-Oliver, J.M.; Pastor, J.M.; Pandal, A.; Trask, N.; Baldwin, E.; Schmidt, D.P. Diesel Spray CFD Simulation Based on the Σ -Y Eulerian Atomization Model. *At. Sprays* **2013**, *23*, 71–95. [[CrossRef](#)]
20. Jordan, P.; Colonius, T. Wave Packets and Turbulent Jet Noise. *Annu. Rev. Fluid Mech.* **2013**, *45*, 173–195. [[CrossRef](#)]
21. Kalugin, M.D.; Korchagova, V.N.; Kraposhin, M.V.; Marchevsky, I.K.; Moreva, V.S. Using big analytics tools in performance of gas dynamics and acoustics tasks. *Her. Bauman Mosc. State Tech. Univ. Ser. Nat. Sci.* **2018**, *3*, 32–47. [[CrossRef](#)]
22. Salehian, S.; Mankbadi, R.R. Simulation of rocket launch noise suppression with water injection from impingement pad. *Int. J. Aeroacoustics* **2020**, *19*, 207–239. [[CrossRef](#)]
23. Pourhashem, H.; Kumar, S.; Kalkhoran, I.M. Flow field characteristics of a supersonic jet influenced by downstream microjet fluidic injection. *Aerosp. Sci. Technol.* **2019**, *93*, 105281. [[CrossRef](#)]
24. Rajput, P.; Kumar, S. Use of downstream fluid injection to reduce subsonic jet noise. *Int. J. Aeroacoustics* **2019**, *18*, 554–574. [[CrossRef](#)]
25. Fukuda, K.; Tsutsumi, S.; Shimizu, T.; Takaki, R.; Ui, K. Examination of sound suppression by water injection at lift-off of launch vehicles. In Proceedings of the 17th AIAA/CEAS Aeroacoustics Conference, Portland, OR, USA, 5–8 June 2011.
26. Lew, P.; Najafi-Yazdi, A.; Mongeau, L. Unsteady numerical simulation of a round jet with impinging microjets for noise suppression. *J. Acoust. Soc. Am.* **2013**, *134*, 1982–1989. [[CrossRef](#)]
27. Kraposhin, M.V.; Banholzer, M.; Pfitzner, M.; Marchevsky, I.K. A hybrid pressure-based solver for nonideal single-phase fluid flows at all speeds. *Int. J. Numer. Meth. Fluids* **2018**, *88*, 79–99. [[CrossRef](#)]
28. Kraposhin, M.V.; Smirnova, E.V.; Elizarova, T.G.; Istomina, M.A. Development of a new OpenFOAM solver using regularized gas dynamic equations. *Comput. Fluids* **2018**, *166*, 163–175. [[CrossRef](#)]
29. Elizarova, T.G. *Quasi-Gas Dynamic Equations*; Springer: Berlin/Heidelberg, Germany, 2009.
30. Elizarova, T.G.; Zlotnik, A.A.; Shil'nikov, E.V. Regularized equations for numerical simulation of flows of homogeneous binary mixtures of viscous compressible gases. *Comput. Math. Math. Phys.* **2019**, *59*, 1832–1847. [[CrossRef](#)]
31. Balashov, V.; Savenkov, E.; Zlotnik, A. Numerical method for 3D two-component isothermal compressible flows with application to digital rock physics. *Russ. J. Numer. Anal. Math. Model.* **2019**, *34*, 1–13. [[CrossRef](#)]
32. Putnam, A. Integrable form of droplet drag coefficient. *ARS J.* **1961**, *31*, 1467.
33. O'Rourke, P.J.; Amsden, A.A. *The TAB Method for Numerical Calculation of Spray Droplet Breakup*; SAE: Warrendale, PA, USA, 1987.
34. Aissa, A.; Abdelouahab, M.; Noureddine, A.; Elganaoui, M.; Pateyron, B. Ranz and Marshall correlations limits on heat flow between a sphere and its surrounding gas at high temperature. *Therm. Sci. VINČA Inst. Nucl. Sci.* **2015**, *19*, 1521–1528. [[CrossRef](#)]
35. Brentner, K.; Farassat, F. An analytical comparison of the acoustic analogy and Kirchhoff formulations for moving surfaces. *AIAA J.* **1998**, *36*, 1379–1386. [[CrossRef](#)]
36. Brès, G.A.; Pérot, F.; Freed, D. A fowcs Williams-Hawkings solver for lattice Boltzmann based computational aeroacoustics. In Proceedings of the 16th AIAA/CEAS aeroacoustics conference, Stockholm, Sweden, 7–9 June 2010; p. 3711.
37. Epikhin, A.; Evdokimov, I.; Kraposhin, M.; Kalugin, M.; Strijhak, S. Development of a dynamic library for computational aeroacoustics applications using the OpenFOAM open source package. *Procedia Comput. Sci.* **2015**, *66*, 150–157. [[CrossRef](#)]
38. libAcoustics Library. Available online: <https://github.com/unicfdlab/libAcoustics> (accessed on 10 June 2021).
39. Kraposhin, M.; Bovtrikova, A.; Strijhak, S. Adaptation of Kurganov-Tadmor numerical scheme for applying in combination with the PISO method in numerical simulation of flows in a wide range of mach numbers. *Procedia Comput. Sci.* **2015**, *66*, 43–52. [[CrossRef](#)]
40. Epikhin, A.; Kraposhin, M.; Vatutin, K. The numerical simulation of compressible jet at low Reynolds number using OpenFOAM. *E3S Web Conf.* **2019**, *128*, 3. [[CrossRef](#)]
41. Epikhin, A.; Kraposhin, M. Prediction of the free jet noise using quasi-gas dynamic equations and acoustic analogy. *Lect. Notes Comput. Sci.* **2020**, *12143*, 217–227.
42. Liu, A.B.; Mather, D.; Reitz, R.D. Modeling the effects of drop drag and breakup on fuel sprays. *J. Engines* **1993**, *102*, 83–95.
43. Greska, B.; Krothapalli, A. Jet noise reduction using aqueous microjet injection. In Proceedings of the 10th AIAA/CEAS Aeroacoustics Conference, Manchester, UK, 10–12 May 2004; p. 1928.
44. Askarishahi, M.; Salehi, M.; Radl, S. Voidage correction algorithm for unresolved Euler–Lagrange simulations. *Comput. Part. Mech.* **2018**, *5*, 607–625. [[CrossRef](#)]
45. Baars, W.; Tinney, C.; Murray, N.; Jansen, B.; Panickar, P. The effect of heat on turbulent mixing noise in supersonic jets. In Proceedings of the 49th AIAA Aerospace Sciences Meeting including the New Horizons Forum and Aerospace Exposition, Orlando, FL, USA, 4–7 January 2011. AIAA 2011–1029.

-
46. Uzun, A.; Lyrintzis, A.S.; Blaisdell, G.A. Coupling of integral acoustics methods with LES for jet noise prediction. *Int. J. Aeroacoustics* **2004**, *3*, 297–346. [[CrossRef](#)]
 47. Shur, M.; Spalart, P.; Strelets, M. Noise prediction for increasingly complex jets. Part I: Methods and tests. *Int. J. Aeroacoustics* **2005**, *4*, 213–246. [[CrossRef](#)]